Scanning Tunneling Andreev Microscopy of Titanium Nitride Thin Films

Wan-Ting Liao,[1, 2] T. P. Kohler,[1, 3] K. D. Osborn,[1, 4] R. E. Butera,[1] C. J. Lobb,[2, 4] F. C. Wellstood,[2, 4] and M. Dreyer[1]

[1]*Laboratory for Physical Sciences, College Park, Maryland 20740*
[2]*Center for Nanophysics and Advanced Materials, Department of Physics,*
University of Maryland, College Park, Maryland 20742
[3]*Department of Electrical Engineering, University of Maryland, College Park, Maryland 20742*
[4]*Joint Quantum Institute, University of Maryland, College Park, Maryland 20742*
(Dated: November 12, 2019)

We report scanning tunneling microscopy results on 25 and 50 nm thick films of superconducting TiN that show Andreev tunneling behavior at 0.5 K. At most locations on the topographically rough surfaces, we observe tip-sample current-voltage characteristics with a clear superconducting gap, as expected for superconductor-normal (S-N) tunneling through a low-transparency barrier, while in some places, we find a zero-voltage conductance peak, as expected for S-N Andreev tunneling through a highly transparent barrier. Fitting the Blonder-Tinkham-Klapwijk (BTK) model to the conductance data allows an accurate extraction of the TiN superconducting gap Δ, by accounting for local variations in the tip-sample barrier height Z and junction temperature T. From spatial maps of the model parameters, we find that both films show a strong inhomogeneity, with Δ varying by as much as a factor of two from grain to grain. In the thicker film, however, correlations between T, Z, and Δ suggest the grains are thermally isolated, perhaps due to internal stress. We discuss possible mechanisms that could produce these large correlated variations, including local heating and surface contamination, and consider some of the implications for devices made from such films.

I. INTRODUCTION

Thin films of superconducting titanium nitride (TiN) have attracted much recent interest due to their very low microwave loss and high kinetic inductance. This makes TiN attractive for building microwave resonators for applications in quantum computation [1–6] and for constructing superconducting microwave kinetic inductance detectors for x-ray spectroscopy and sub-millimeter-wave astronomy [7–11]. In practice, the microwave loss, superconducting critical temperature T_c, micro-structure, grain size, and stress in TiN all depend on the growth conditions [12–14]. Although measurements of T_c [15] and kinetic inductance [16] provide evidence for a homogeneous material with a uniform gap Δ, atomic scale scanning tunneling microscopy (STM) [17] shows very rough surfaces and small grains which suggests the potential for significant grain-to-grain variations in superconducting properties [18]. Large variations in the gap could provide low-gap regions that act as trapping sites for non-equilibrium quasiparticles [19–21], leading to films with low-loss characteristics. Furthermore, TiN films with high kinetic inductance are likely the result of grains that are weakly coupled together, which would reduce the proximity effect [22] and allow grain-to-grain variations in Δ. Measurements of very thin (5 nm) TiN films have revealed a superconductor-insulator transition and spatially inhomogeneous superconducting gap [23–26], but the situation for thicker films used in resonators is unclear.

Here, we report STM results on superconducting 50 and 25 nm thick TiN films taken at 0.5 K. We observe large variations in the current-voltage characteristics, with a distinct zero-bias conductance peak occurring at some locations. Such peaks are characteristic of Andreev superconductor-normal (S-N) tunneling [27] through a highly transparent barrier, as opposed to conventional S-N quasiparticle tunneling [28, 29] through a low-transparency barrier. Using an analysis based on the Blonder-Tinkham-Klapwijk (BTK) model of Andreev tunneling [30], we extract maps of the superconducting gap Δ, junction temperature T, and barrier height Z which all show relatively large spatial variations. Both films show significant grain-to-grain variations in Δ, as well correlations between the topography, Δ, T, and Z. We examine some mechanisms that could lead to variations in the local temperature and produce these correlations, and conclude with a discussion of some of the potential implications.

II. FILM PREPARATION AND CHARACTERIZATION

Our TiN films were deposited on a high resistivity (100) silicon wafer ($\rho > 20$ k$\Omega \cdot$ cm) [31]. The substrate was pretreated in an O_2 plasma for 30 s before being put into a DC magnetron sputter chamber. During sputtering the substrate was heated to $500°$C and 400 W of rf power was applied to a 7.6 cm diameter Ti target. A pressure of 3.5 mTorr was maintained while flowing Ar and N_2 gas at 15 and 10 SCCM, respectively. Resistive measurements gave $T_c = 4.7$ K for the 50 nm thick film while the 25 nm film had $T_c = 3.6$ K. From T_c, we find a superconducting coherence length $\xi \approx 18$ nm for the 50 nm thick film and $\xi \approx 15$ nm for the 25 nm thick film. Resonators made from the 50 nm film showed an internal quality factor of $Q_i = 2 \times 10^5$, whether or not an O_2 pretreatment was used, while the 25 nm thick film had $Q_i = 1.5 \times 10^4$ with an O_2 pretreatment, compared

to $Q_i = 2\times10^5$ without O_2 pretreatment. For the 50 nm thick film $k_F l \approx 24$, while $k_F l \approx 14$ for the 25 nm film, where k_F is the Fermi wavelength and l is the electron mean free path [32]. Based on these values, neither film is beyond the Ioffe-Regel limit [33] and both are weakly disordered.

Prior to imaging with the STM, each film was mounted on a sample stud [34], sonicated in isopropanol for five minutes and transferred to a custom UHV system [34]. The sample was heated to 300°C and the surface was cleaned by sputtering using 750 eV Ar ions for 60 minutes. We avoided using higher temperatures during cleaning because we found that heating TiN films above 400°C caused T_c to decrease substantially. The sample was then transferred without breaking vacuum to the cold stage of a mK STM [34]. A vanadium (V) tip was used to image the 50 nm thick TiN film, while a niobium tip [35] was used to image the 25 nm thick TiN film.

Figure 1 shows topographic images of the 50 and 25 nm TiN films. Both films are very granular, with maximum grain diameters of about 20 nm and 10 nm for the 50 nm thick film and 25 nm thick film, respectively. The surface roughness is 4 nm for the 50 nm thick film and 2 nm for the 25 nm thick film.

III. ANDREEV TUNNELING CHARACTERISTICS

Figure 2(a) shows an STM topographic map of a small 42 nm × 42 nm region (256 × 256 pixels) on the 50 nm thick TiN film. This image was acquired at 0.5 K using
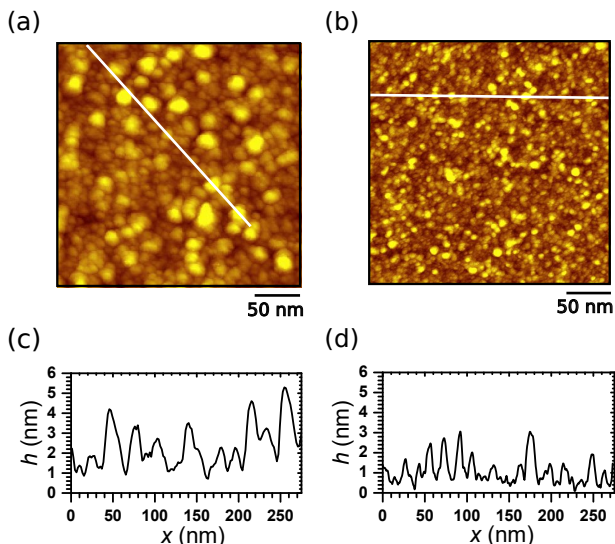

FIG. 1. (a) Topographic image of 50 nm thick TiN film and (b) 25 nm thick TiN film. (c) Line section along white line in (a) showing topographic height versus distance x of grains in the 50 nm thick film. (d) Line section along white line in (b) showing grain topography for the 25 nm thick film.
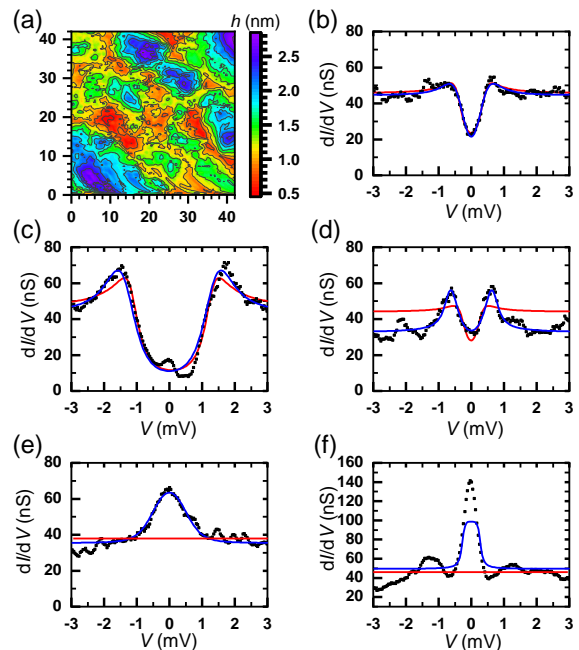

FIG. 2. (a) Fine scale (42 nm × 42 nm) topographic map of 50 nm thick TiN film, acquired at 0.5 K using a V tip. (b)-(f) Representative measured conductance dI/dV versus voltage V (black points) at selected locations as well as fits to the BTK model (blue) and Dynes model (red). The parameters for the BTK and Dynes fits, and the locations where the curves were taken, are listed in Table I.

the V tip with a voltage bias of 4 mV and a tunneling current of 100 pA. In this false color image, the blue and purple regions are nominally 1 to 2 nm higher than the red and yellow regions. As the topographic image was being acquired, the scan was paused at every other point, feedback was briefly turned off, and I-V curves were measured by sweeping the bias voltage V from 4 to -4 mV while recording the tunnel current I. Conductance dI/dV versus V curves were obtained simultaneously by adding a small ac modulation voltage (140 μV) to the voltage bias and using a lock-in amplifier to extract the ac signal from the tunnel current. The resulting spectroscopy map size is 128 × 128 pixels.

Figures 2(b)-(f) show dI/dV $vs.$ V curves at five selected locations in Fig. 2(a) with the locations given in Table I. The range of behavior is striking. Qualitatively, Fig. 2(b) shows a clearly recognizable superconducting gap, as expected for S-N tunneling through a conventional low-transparency barrier [36]. However the leakage current at low voltages is much larger than what is expected for conventional S-N tunneling at $k_B T \ll \Delta$. Figure 2(c) shows similar behavior, but with more prominent coherence peaks, a larger gap and less sub-gap leakage current. Figure 2(d) shows a more extreme deviation from conventional S-N tunneling: a gap and coherence peaks are clearly visible, but the conductance at $V = 0$ is almost the same as at high voltage. In contrast, Fig. 2(e)

TABLE I. Coordinates (x, y) and corresponding superconducting gap Δ, temperature T, and barrier height Z from fitting the BTK model of Eq. (1) to the conductance curves in Figs. 2(b)-(f). Also shown are Δ and broadening parameter Γ from fitting the Dynes model, Eq. (2), to the data.

		BTK			Dynes	
Location (x, y)(nm)		Δ (meV)	T (K)	Z	Δ (meV)	Γ (meV)
(b)	(36.42, 9.19)	0.35	1.95	3.15	0.395	0.235
(c)	(26.91, 13.78)	1.39	2.44	1.44	1.27	0.34
(d)	(2.63, 5.25)	0.66	0.94	0.56	0.287	0.237
(e)	(8.20, 36.09)	0.44	2.60	0.003	-	-
(f)	(34.78, 13.45)	0.25	0.42	0.002	-	-

shows a distinct peak in the conductance at zero bias, reaching about two times the value at high voltage. This is what is expected from S-N tunneling through a highly transparent barrier when Andreev reflection [27, 30] is taken into account. Reexamining the curve in Fig. 2(d), we note it is qualitatively consistent with Andreev tunneling through a barrier that is of intermediate transparency. Finally, Fig. 2(f) shows a conductance curve with an anomalously high zero-bias conductance peak.

Although the data were acquired below T_c of both TiN and V, we find S-N tunneling characteristics because the V tip easily picks up debris from the rough TiN surface, which results in an effectively normal tip. For our spectroscopy measurements in particular, we needed to use a relatively low sample bias (< 5 mV). This leads to a junction resistance of order 50 MΩ and places the tip closer to the sample than would be the case for a typical STM sample bias of about 1 V and junction resistance ~ 1 GΩ. We note that we sometimes observed superconductor-insulator-superconductor (S-I-S) behavior at certain locations, and occasionally over relatively large portions of the surface (see Supplementary Material [37]). However, superconducting tips had the tendency to change during acquisition of the spectroscopic map, making this data more challenging to analyze. This suggests that the characteristic in Fig. 2(c) may be due to S-I-S tunneling, with the large apparent gap being the sum of the gaps of the tip and sample. Since relatively few points in Fig. 2(a) showed S-I-S behavior, we ignore this possibility in the following analysis.

We fit the conductance data using the BTK model of Andreev reflection [30] at an S-N interface. The key variable in the model is the barrier height parameter Z of the interface. For $Z \ll 1$, the interface is very transparent, while for $Z \gg 1$, the barrier has a low transparency and one recovers the conventional S-N tunneling limit [28]. The BTK model conductance can be expressed as [30]

$$\frac{\mathrm{d}I}{\mathrm{d}V} = A_0 \times \int_{-\infty}^{\infty} \frac{\partial f_0(E - eV)}{\partial V} \big(1 + A(E) - B(E)\big) \mathrm{d}E. \quad (1)$$

Here $f_0(E)$ is the Fermi function $1/(e^{E/k_B T} + 1)$, which is dependent on the temperature T and k_B is the Boltzmann constant. $A(E)$ is the probability of the Andreev reflection at the S-N interface, $B(E)$ is the probability for the reflection of normal electrons of energy E, and

$A_0 = (1 + Z^2)/(eR_N)$ where R_N is the normal state resistance of the junction. $A(E)$ and $B(E)$ depend on the barrier height Z and the superconducting gap Δ [30], as summarized in Table II.

We evaluated Eq. (1) numerically and varied Δ, T, and Z to obtain the best fit to the measured $\mathrm{d}I/\mathrm{d}V$ vs. V curve at each location. The blue curves in Figs. 2(b)-(f) show the resulting BTK fits, with the fit parameters given in Table I. We find good qualitative agreement except for the curve in Fig. 2(f).

For comparison, the red curves in Figs. 2(b)-(f) show fits to the Dynes gap function for a conventional high-barrier tunnel junction [29]. In this case, we can write

$$\frac{\mathrm{d}I}{\mathrm{d}V} \propto \mathrm{Re}\left(\frac{E - i\Gamma}{\sqrt{(E - i\Gamma)^2 - \Delta^2}}\right), \quad (2)$$

where Γ is the broadening parameter. Comparing the measurements (black) to the Dynes fits (red) in Figs. 2(b)-(f), we see reasonable fits to Eq. (2) for Figs. 2(b) and (c), but qualitatively very poor fits in Figs. 2(d)-(f), where the best fits yield $\Delta \approx 0$.

Examining the best fit parameters Δ, Z, and T in Table I obtained from the BTK model, we see large differences in Z at the different locations. For example, for Fig. 2(b) we found $Z = 3.15$, which is somewhat large compared to 1, indicating the junction is not far from being in the conventional S-N tunneling limit [36]. In contrast, the curve in Fig. 2(d) yielded $Z = 0.56$, which indicates a fairly transparent barrier. The BTK fits in Figs. 2(e) and (f) yielded $Z \approx 0.003$ and $Z \approx 0.002$, respectively, which indicates a very transparent barrier.

TABLE II. Functions $A(E)$ and $B(E)$ in the BTK model [30]. $A(E)$ is the probability of an electron in the normal metal undergoing Andreev reflection when incident on the N-S interface. $B(E)$ is the probability of an incident electron of energy E undergoing ordinary reflection at the N-S interface. Z is the barrier height parameter and Δ is the superconducting gap.

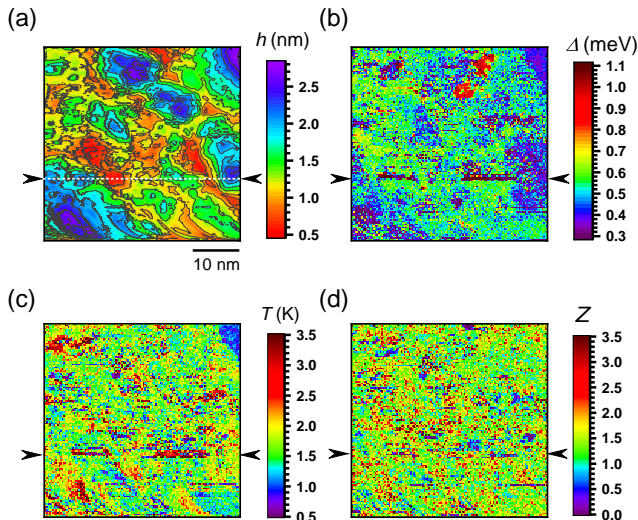|	$A(E)$	$B(E)$
$E > \Delta$	$\frac{\Delta^2}{[E + \sqrt{E^2 - \Delta^2}(1 + 2Z^2)]^2}$	$\frac{4Z^2(1 + Z^2)(E^2 - \Delta^2)}{[E + \sqrt{E^2 - \Delta^2}(1 + 2Z^2)]^2}$
$E < \Delta$	$\frac{\Delta^2}{[E^2 + (\Delta^2 - E^2)(1 + 2Z^2)^2]}$	$\frac{4Z^2(1 + Z^2)(\Delta^2 - E^2)}{[E^2 + (\Delta^2 - E^2)(1 + 2Z^2)^2]}$

FIG. 3. (a) False color map showing topography of the 50 nm thick TiN film (same as Fig. 2(a)). (b) Corresponding maps of superconducting gap Δ, (c) temperature T, and (d) barrier height parameter Z, found by fitting the conductance curve at each location to the BTK model, Eq. (1). The dark blue regions in the Z map indicate locations where there is a zero-bias conductance peak.

FIG. 4. False color plot of conductance dI/dV versus position x and voltage V along the line cut indicated by black arrows in Fig. 3.

We note in particular that the zero-bias peak of a highly transparent S-N junction in Fig. 2(e) is quantitatively reproduced by the BTK fit, with sensible parameters.

Our application of the BTK model assumes a single channel with well-defined Z, Δ, and T. Better fits could be obtained by allowing for two or more channels with different Z values [38]. Also, the BTK fit in Fig. 2(f) does not fully capture the zero-bias conductance peak, possibly suggesting that mid-gap states are present [39] or that some other physics is occurring. Although only a few sample curves are shown in Fig. 2, the range of behavior is typical and encompasses S-N Andreev tunneling through barriers with a wide range of transparency. Although the fits to the BTK model are not perfect, they much more faithfully reproduce the full range of behavior present in our data than fitting to the Dynes model. Thus, we conclude that Andreev effects are important in interpreting the STM data from our TiN samples and that using a Dynes model here would potentially result in incorrect interpretations, including mistaking high transparency regions for regions with large broadening or zero gap.

IV. Δ, T, Z AND h CORRELATION

Figure 3(a) again shows the topographic image of the 50 nm TiN film, while Figs. 3(b)-(d) show corresponding maps of Δ, T, and Z obtained from fitting the BTK model to each conductance curve. First, note that there are spatially-correlated variations in all four maps, but
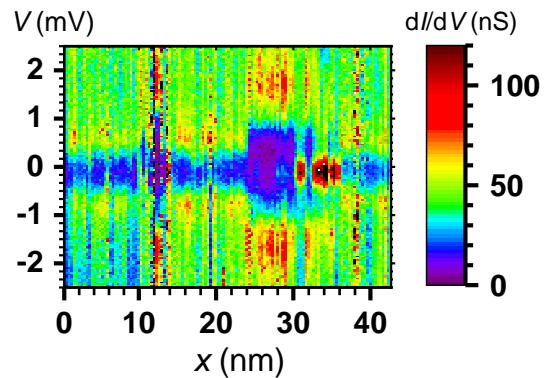
they are most obvious in the topography and gap. Comparing the topography in Fig. 3(a) to the Δ map in Fig. 3(b), one sees a distinct correspondence between the colors – topographically high points (blue) in Fig. 3(a) correspond to small values of Δ (blue) in Fig. 3(b). Similar but much less pronounced spatially correlated variations in T are evident in Fig. 3(c), with higher points (blue) tending to give higher temperature (red), e.g. in the upper left and lower left corners. A notable exception to this trend occurs in the upper right hand corner where successive scan lines show a contiguous high region (blue) with a low temperature (blue). This appears to be a well-defined grain. We note in particular that Δ changes abruptly at the left boundary of this region, on a scale that is much smaller than the coherence length ξ, even taking into account the mean free path [32]. This suggests the presence of a grain-to-grain barrier and relatively poor coupling of superconducting pairs across the boundary. Finally, correlations between topography and Z are also present, but they are much less obvious due to large random point-to-point variations in Z. Also evident in Fig. 3(d) are some small patches of dark blue, indicating $Z \approx 0$. These are the points that show a zero-bias conductance peak.

Another striking feature of these maps is the relatively large size of the variations, with the respective scales covering 0.3 meV $< \Delta <$ 1.1 meV, 0.5 K $< T <$ 3.5 K, and $0 < Z < 3.5$. To verify that large spatially-correlated variations in the gap are directly visible in the raw data, Fig. 4 shows a false color plot of dI/dV vs. V along a line cut indicated by arrows in Fig. 3. Distinct regions are clearly visible where the superconducting gap differs by a factor of 2. Again the transition from low to high gap appears to be abrupt on the nm scale, suggesting variations between disconnected grains. One also sees a section with a prominent zero-bias conductance peak (red), consistent with Andreev effects in an S-N junction with a high transparency.

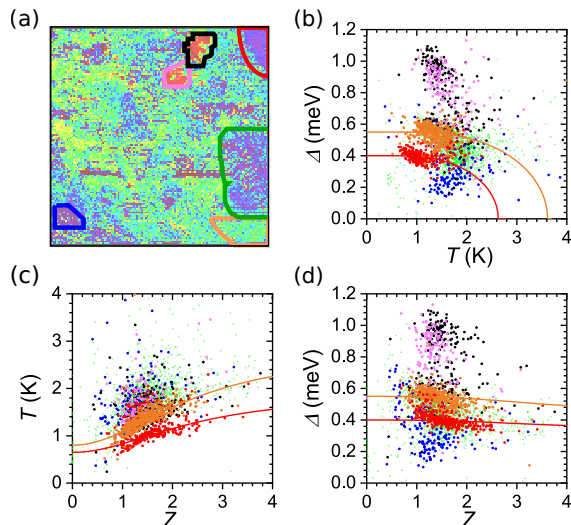The data of Fig. 4 were also used to estimate the un-

FIG. 5. (a) Gap map of 50 nm film (same as Fig. 3(b)) with six regions outlined (pink, black, red, orange, blue, green). (b) Δ as a function of T with color of points matching regions outlined in (a). The red and orange curves are fits to the BCS model for $\Delta(T)$ with $\Delta(0) = 0.4$ meV and $\Delta(0) = 0.55$ meV, respectively. (c) T as a function of Z. The red curve shows a fit to heating model Eq. (4) with parameters $T_n = 0.4$ K, $\delta T = 1.5$ K, and $r = 5$, while the orange curve is a fit with $T_n = 0.4$ K, $\delta T = 2.4$ K, and $r = 5$. (d) Scatter plot of Δ vs. Z for the points in the six regions. The red and orange curves are drawn using $\Delta(T(Z))$ with parameters listed in (b) and (c).

certainties of the fitting parameters. As the spatial separation between successive points was only 3 Å, their conductance curves should tend to be described by similar parameters. Although some of the larger variations are clearly due to actual changes in the gap, most of the smaller point-to-point differences appear to be random noise. We find the variation of the gap in this line section gives $\sigma_\Delta = 0.04$ meV. Similarly, point-to-point differences in the T and Z fit parameters along the same scan line in Fig. 4 yielded the uncertainty of the temperature and barrier height, $\sigma_T = 0.2$ K and $\sigma_Z = 0.2$, respectively (see Supplementary Material [37] for a detailed analysis).

The fact that our TiN film shows large local variations in Δ is perhaps not surprising given the granular nature of the films. Also, variations in barrier height Z are not surprising because they may simply be due to surface contamination or local Ar ion damage created while cleaning the film. In contrast, a remarkable but unexpected feature of these maps is that the topography is correlated to T and that there are correlations between Δ, T, and Z.

To help reveal these correlations, in Fig. 5(a) we have highlighted six regions of interest in the superconducting gap map of the 50 nm TiN film. The red region in the upper right corner contains the contiguous region noted above with a small superconducting gap. The black and

pink regions (top center) show a higher gap. The orange area in the lower right corner shows a Δ that is near the average Δ of the film. The green and blue regions are two other contiguous low gap areas that stand out from neighboring regions.

Figure 5(b) shows the corresponding plot of the superconducting gap Δ vs. the temperature T for all the points in the selected regions, with each point's color corresponding to its region. The different regions tend to be clustered in the plot rather than being randomly distributed; the red and the orange regions in particular form distinct clouds. The orange and red curves in Fig. 5(b) show fits to the Bardeen-Cooper-Schrieffer (BCS) theory [40] for $\Delta(T)$ with $\Delta(0) = 0.4$ meV for the red curve and $\Delta(0) = 0.55$ meV for the orange curve. Despite the substantial variation in temperature, we see that the BCS theory appears to be consistent with the relatively constant gap seen in the red and orange regions.

Figure 5(c) shows the corresponding plot of temperature T versus Z for the points in the regions highlighted in Fig. 5(a). Again we see well-defined clustering of points for the red and orange regions. Surprisingly, the temperature reaches 1 or 2 K as the barrier height parameter Z grows from 1 to 2. Qualitatively, this behavior is consistent with the tip acting as a heat sink. If the barrier height Z is small, the tip and the sample are thermally well-coupled and heat generated by the tunneling current can either flow back to the tip or flow out through the sample. In contrast, for a higher barrier parameter Z, heat deposited locally in the sample can only flow out through the sample and not through the tip, resulting in a higher temperature.

To quantitatively describe this behavior, we used the simple heating model depicted in Fig. 6. We consider
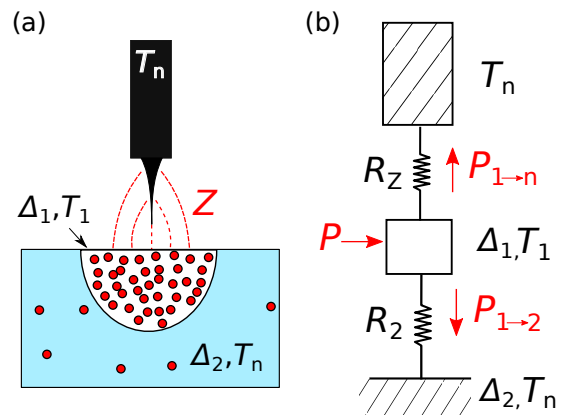

FIG. 6. Illustration showing a normal metal STM tip near the surface of a superconducting sample that has a low-gap region Δ_1 in a high-gap region Δ_2. We assume that most of the quasiparticles (red) are trapped in the low-gap region and that the tip and the high-gap region are both at temperature T_n. In the steady state, the power dissipated in the low-gap region at temperature T_1 is equal to the heat flow $P_{1\to2} + P_{1\to n}$.

tunneling into a small region on the surface with a gap Δ_1 lower than the surrounding area with gap Δ_2, e.g. a grain with a lower gap. When current I is flowing through the STM junction at bias voltage V, power IV will be dissipated and quasiparticles will be injected into the low-gap region Δ_1. If $\Delta_2 - \Delta_1 \gg k_B T$, the quasiparticles will be trapped in the low gap region and consequently the number of quasiparticles and temperature will increase until steady state is reached. For simplicity we assume that all of the power is deposited in the low-gap region and that heat then flows out to the tip or to the high-gap region. The heat flow is proportional to the temperature difference $T_1 - T_n$ between the Δ_1 region and the tip or substrate, which are both at temperature $T_n \approx 0.5$ K. In the steady state we can then write

$$P = IV = \alpha(T_1 - T_n)/(1 + Z^2) + \beta(T_1 - T_n). \quad (3)$$

The first term on the right represents heat flow from low-gap region Δ_1 region to the tip, $1/(1+Z^2)$ is the barrier transparency between the tip and the sample, and α is a thermal transport coefficient which depends on details of the tip, such as its area. The second term represents heat flow from the Δ_1 region to the Δ_2 region in the sample, where β is another thermal transport coefficient that depends on details of the low-gap and high-gap regions, including their contact area and how well connected they are.

Solving Eq. (3) for the temperature T_1 of the Δ_1 region gives

$$T_1 = T_n + \frac{\delta T}{\frac{r}{1+Z^2} + 1}, \quad (4)$$

where $r = \alpha/\beta$ and $\delta T = IV/\beta$. The red curve in Fig. 5(c) shows a fit of Eq. (4) to the red data points with $T_n = 0.4$ K, $\delta T = 1.5$ K and $r = 5$, while the orange curve shows a fit to the orange points with $T_n = 0.4$ K, $\delta T = 2.4$ K and $r = 5$. The curves capture the qualitative behavior of $T(Z)$ in their respective regions and the larger value of δT in the orange region is consistent with it being less thermally connected to the surrounding material. We note that the model does not require that the tunneling be into a region with a gap that is smaller than the surrounding matrix. It is sufficient that there is a barrier to quasiparticle flow between the region and its surroundings.

Given $\Delta(T)$ and $T(Z)$, we can evaluate $\Delta(T(Z))$ without any additional parameters. The red and orange curves in Fig. 5(d) show the resulting functions $\Delta(Z)$ are in reasonable correspondence with the data. An important implication of this region-specific agreement with the model is that the red and orange regions have distinct gap and thermal conductance, as expected for isolated grains. The points in the green and blue regions are more dispersed but appear to behave similarly to the red and orange regions. The pink and black points form a distinct cluster at high Δ, possibly because of S-I-S tunneling, as noted above.
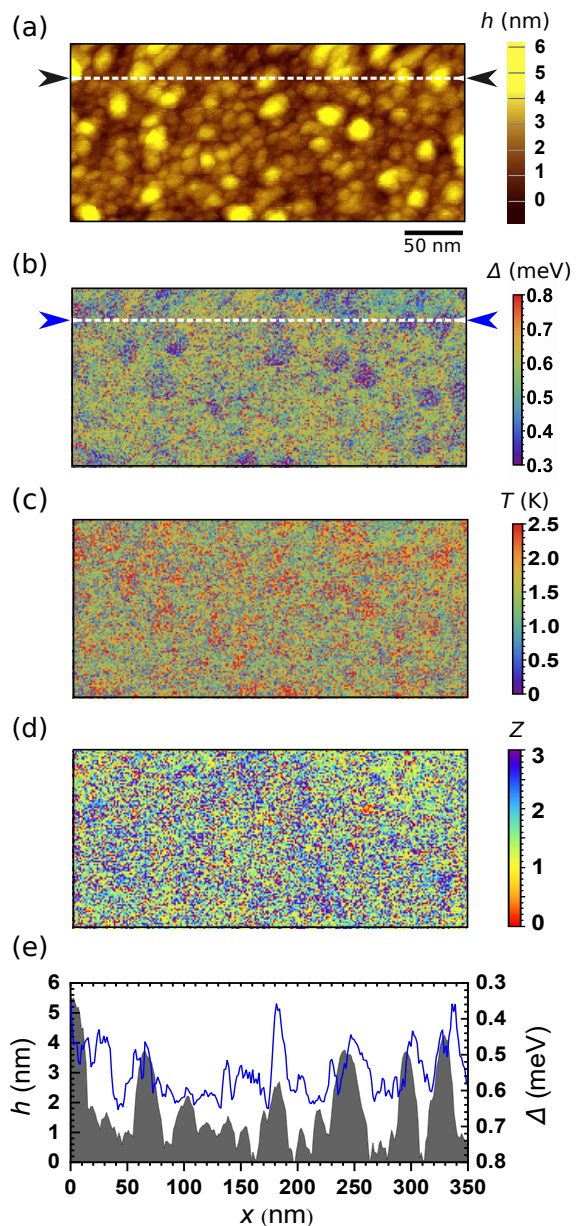

FIG. 7. (a) Large scale topography of the 50 nm thick TiN film taken at 100 pA tunneling current and 4 mV bias showing a rough granular surface. (b) Corresponding map of gap Δ, (c) temperature T, and (d) barrier height parameter Z from fitting the BTK model to the conductance curves. (e) Line sections through (a) and (b) showing anti-correlation between the gap (blue) and topography (gray). Note reversed scale for Δ, i.e. large gaps correspond to small h.

V.   50 nm AND 25 nm FILM COMPARISON

Correlations between h, Δ, T, and Z are also evident in larger scale spectroscopic maps of the 50 nm and 25 nm thick films. Figure 7(a) shows a 350×160 nm^2 topographic image of the 50 nm film, again acquired at 0.5 K with the V tip. For this image, we used a voltage bias

of $V = 4$ mV and a tunneling current of $I = 100$ pA. The resulting topographic map had 256×113 points and we acquired I-V and dI/dV-V spectra at each location. Figures 7(b), (c), and (d) show the corresponding maps of the superconducting gap Δ, temperature T, and barrier height Z obtained by fitting the BTK model, Eq. (1), to the conductance data. Gray points in the map indicate locations where we did not obtain a good fit (see Supplementary Material [37]) typically due to excessive noise or drift. Comparing the topography to the Δ and T maps, we again see clear correlations: the higher the grain, the smaller the superconducting gap and the higher the temperature. In contrast, the Z map appears uniformly noisy and relatively featureless. Figure 7(e) shows line sections through the topographic image (gray) and the gap map (blue). Examining the plot, we see again that Δ is strongly anti-correlated with surface height (note the reversed scale for Δ).

Similar behavior is seen for the 25 nm thick TiN film. Figure 8(a) shows a 280 nm $\times$ 112 nm topographic image taken at $T = 0.5$ K with a Nb tip. Spectroscopy data were taken at 256×101 locations; I $vs.$ V and dI/dV $vs.$ V were recorded simultaneously. Figures 8(b)-(d) show the corresponding maps of Δ, T, and Z, extracted from the BTK model. Examining the topographic image (Fig. 8(a)) and Δ map (Fig. 8(b)), we again see a distinct anti-correlation, with the higher grains having smaller superconducting gap. To see this more clearly, Fig. 8(e) shows a line cut through the surface topography (gray) and the BTK gap Δ map (blue). As with the 50 nm thick film, the 25 nm film shows a remarkable anti-correlation between surface height and gap.

Unlike what we found in the 50 nm film, the temperature map for the 25 nm film (see Fig. 8(c)) shows little obvious correlation with the topography. On the other hand, the Z map (see Fig. 8(d)) reveals that high Z regions (blue) tend to have lower superconducting gap (blue in Fig. 8(b)). This behavior was not obvious in the 50 nm thick film in Fig. 7(d), but does show up weakly in the $\Delta(Z)$ plot in Fig. 5(d).

To better understand the overall variation of the gap in the 50 nm thick film, the blue curve in Fig. 9(a) shows the histogram of gap values $\Delta(T)$ obtained from Fig. 7(b). In principle, the spread in the values of the observed gap could be due to variations in the junction temperature. To explore this possibility, the red curve in Fig. 9(a) shows the corresponding histogram of $\Delta(0)$ calculated from the BCS theory using the $\Delta(T)$ and T values extracted from the BTK fits. The resulting distribution has a full-width at half maximum (FWHM) of about 0.15 meV, which is remarkably large as it is about 25 % of the average gap value of 0.6 meV. Since the $\Delta(0)$ and $\Delta(T)$ histograms are nearly identical, we conclude that the large variations in the gap are not caused by variations in the temperature but are due to local variations in $\Delta(0)$ in the TiN film.

Figure 9(b) shows the corresponding histograms of $\Delta(T)$ and $\Delta(0)$ for the 25 nm film from Fig. 8(b), which
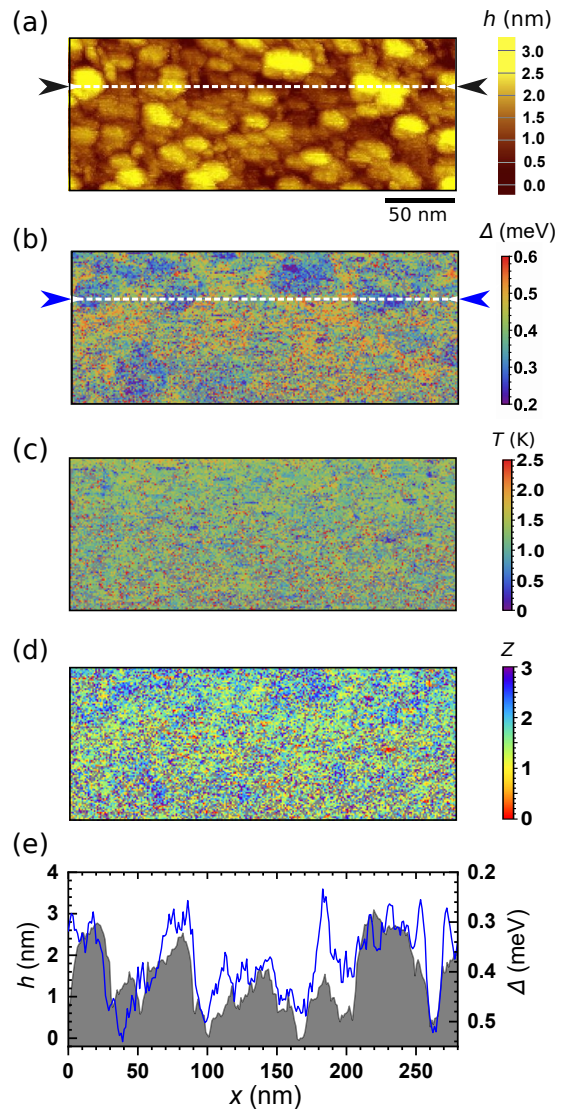

FIG. 8. (a) Topography of the 25 nm thick TiN film taken at I=100 pA and V=3 mV. There is some distortion in this image due to the tip shape. (b) Corresponding map of gap Δ, (c) temperature T, and (d) barrier parameter Z extracted from fits to the BTK model. (e) Line sections through (a) and (b) showing anti-correlation between the gap Δ (blue) and the topography h (gray). Note reversed scale for Δ, $i.e.$ large gaps correspond to small h.

shows an even wider distribution; the FWHM is about 0.25 meV or more than 50 % of the average gap value of 0.42 meV. We note that the average gap values for the 25 nm film (0.42 meV) and the 50 nm (0.6 meV) are only qualitatively consistent with resistive measurements of T_c. For a BCS superconductor, the 4.7 K transition temperature of the 50 nm film would imply a gap of about 0.72 meV and the T_c of 3.6 K for the 25 nm thick film gives $\Delta(0) = 0.55$ meV (see arrows in Fig. 9).

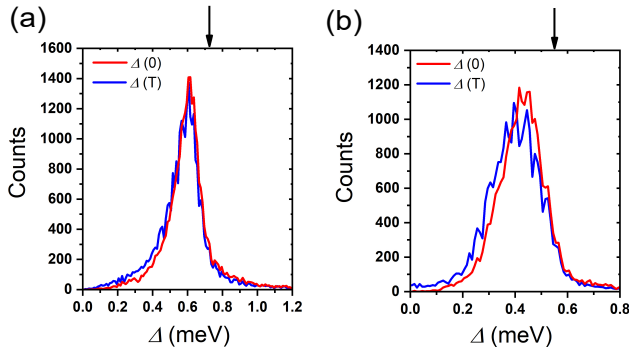Although the gap maps show clear grain-to-grain vari-

FIG. 9. (a) The blue curve shows a histogram of the superconducting gap from the gap map in Fig. 7(b) for the 50 nm thick film. The red curve shows a histogram of the corresponding superconducting gap at temperature $T = 0$ K obtained using the BCS model and the extracted values of $\Delta(T)$ and T. Black arrows indicate Δ from the measured T_c of the films. (b) Corresponding histograms of $\Delta(T)$ (blue) and $\Delta(0)$ (red) for the gap map in Fig. 8(b) for the 25 nm thick film.

ations that correlate with topography, the detailed anti-correlated variation of Δ with h, as seen in Fig. 7(e) and Fig. 8(e), is puzzling. Also puzzling are the grain-to-grain variations in T that occur in the thick film (see Fig. 7), but not in the thin film (see Fig. 8). We propose a possible mechanism that could be generating these disparate correlations in Δ, Z, and h. During the Ar ion cleaning, isolated grains could charge up, repelling incoming ions and leaving dirtier disconnected regions that protrude from the surface. Contamination could lead to higher Z and smaller Δ. Since isolated grains would also tend to be more thermally disconnected, it would produce a higher temperature T when electrical power is dissipated during spectroscopic measurements.

Given that TiN films can have large internal stress [41], leading to more cracking in thicker films, it is not surprising that the 50 nm film could contain more grains which are poorly connected thermally to the rest of the film. In contrast, the 25 nm film thick film shows distinct grains in the gap map and topography but relatively featureless variations in T, consistent with the grains being well-connected thermally. Instead we see a correlation between Z and Δ which could indicate surface damage or contamination that causes an increase in the barrier

height Z and also suppresses Δ.

VI. CONCLUSION

In conclusion, we used an STM to image 50 and 25 nm thick TiN films at 0.5 K. The rough granular surfaces show large variations in the superconducting gap that are anti-correlated with the topography. The BTK model of Andreev reflection yields qualitatively better fits to the conductance characteristics than fitting to the Dynes model. It also allows us to extract temperature and barrier height maps, and accounts for distinct Andreev features in the spectroscopy that occur for highly transparent tunnel barriers. We observe distinct grain-to-grain variations in Δ and T as well as correlations between Δ, T, and Z. Using a simple heating model, we argue that locations with a larger barrier height parameter Z should have a higher temperature T, as observed. By combining the heating model and the BCS theory, we obtained a functional dependence of the gap Δ on T and Z which captured the qualitative behavior in selected regions.

Finally we note that the polycrystalline nature and wide variations in gap could potentially impact the microwave properties of the TiN films [6, 42]. The rough surface is a potential host for two level system (TLS) defects and contamination [43, 44]. The low gap regions could act as traps for non-equilibrium quasiparticles [19–21], leading to the low loss observed in this material. Further research into the growth, cleaning, and surface characterization of TiN are of considerable interest. Our Andreev based technique could also be used to investigate other granular thin-films, such as oxygen-doped aluminum [45] as well as other inhomogeneous superconductors [46], where similar issues are likely to arise.

VII. ACKNOWLEDGMENTS

[1] B. Foxen, J. Y. Mutus, E. Lucero, R. Graff, *et al.*, Quantum Sci. Technol. **3**, 014005 (2018).

[2] J. B. Chang, M. R. Vissers, A. D. Crcoles, M. Sandberg, J. Gao, D. W. Abraham, J. M. Chow, J. M. Gambetta, M. B. Rothwell, G. A. Keefe, M. Steffen, and D. P. Pappas, Appl. Phys. Lett. **103**, 012602 (2013).

[3] M. R. Vissers, J. S. Kline, J. Gao, D. S. Wisbey, and D. P. Pappas, Appl. Phys. Lett. **100**, 082602 (2012).

[4] M. R. Vissers, J. Gao, D. S. Wisbey, D. A. Hite, C. C. Tsuei, A. D. Corcoles, M. Steffen, and D. P. Pappas, Appl. Phys. Lett. **97**, 232509 (2010).

[5] J. M. Sage, V. Bolkhovsky, W. D. Oliver, B. Turek, and P. B. Welander, J. Appl. Phys. **109**, 063915 (2011).

[6] E. F. C. Driessen, P. C. J. J. Coumou, R. R. Tromp, P. J. de Visser, and T. M. Klapwijk, Phys. Rev. Lett. **109**, 107003 (2012).

[7] J. Gao, M. R. Vissers, M. Sandberg, D. Li, H. M. Cho, C. Bockstiegel, B. A. Mazin, H. G. Leduc, S. Chaudhuri, D. P. Pappas, and K. D. Irwin, J. Low Temp. Phys. **176**, 136 (2014).

[8] H. G. Leduc, B. Bumble, P. K. Day, *et al.*, Appl. Phys. Lett. **97**, 102509 (2010).

[9] P. Diener, H. G. Leduc, S. J. C. Yates, Y. J. Y. Lankwarden, and J. J. A. Baselmans, J. Low Temp. Phys. **167**, 305 (2012).

[10] T. Cecil, A. Miceli, L. Gades, A. Datesman, O. Quaranta, V. Yefremenko, V. Novosad, and B. Mazin, Physics Procedia **37**, 697 (2012), Proc. of the 2nd Int. Conf. on Techn. and Instrum. in Part. Phys. (TIPP 2011).

[11] O. Noroozian, P. K. Day, B. H. Eom, H. G. Leduc, and J. Zmuidzinas, IEEE Trans. Microwave Theory and Tech. **60**, 1235 (2012).

[12] D. Edström, D. G. Sangiovanni, L. Hultman, I. Petrov, J. E. Greene, and V. Chirita, J. Appl. Phys. **121**, 025302 (2017).

[13] S. Ohya, B. Chiaro, A. Megrant, C. Neill, R. Barends, Y. Chen, J. Kelly, D. Low, J. Mutus, P. J. J. OMalley, *et al.*, Supercond. Sci. and Technol. **27**, 015009 (2014).

[14] A. Shearrow, G. Koolstra, S. J. Whiteley, N. Earnest, P. S. Barry, F. J. Heremans, D. D. Awschalom, E. Shirokoff, and D. I. Schuster, Appl. Phys. Lett. **113**, 212601 (2018).

[15] M. R. Vissers, J. Gao, J. S. Kline, M. Sandberg, M. P. Weides, D. S. Wisbey, and D. P. Pappas, Thin Solid Films **548**, 485 (2013).

[16] P. Diener, H. Schellevis, and J. J. A. Baselmans, Appl. Phys. Lett. **101**, 252601 (2012).

[17] G. Binnig and H. Rohrer, Surf. Sci. **126**, 236 (1983).

[18] B. W. Karr, I. Petrov, P. Desjardins, D. G. Cahill, and J. E. Greene, Surf. Coat. Technol. **94–95**, 403 (1997).

[19] D. J. Goldie, N. E. Booth, C. Patel, and G. L. Salmon, Phys. Rev. Lett. **64**, 954 (1990).

[20] J. P. Pekola, D. V. Anghel, T. I. Suppula, J. K. Suoknuuti, A. J. Manninen, and M. Manninen, Appl. Phys. Lett. **76**, 2782 (2000).

[21] M. Taupin, I. M. Khaymovich, M. Meschke, A. S. Melnikov, and J. P. Pekola, Nat. Commun. **7**, 10977 (2016).

[22] H. Meissner, Phys. Rev. **117**, 672 (1960).

[23] T. I. Baturina, A. Y. Mironov, V. M. Vinokur, M. R. Baklanov, and C. Strunk, Phys. Rev. Lett. **99**, 257003 (2007).

[24] B. Sacépé, T. Dubouchet, C. Chapelier, M. Sanquer, M. Ovadia, D. Shahar, M. Feigelman, and L. Ioffe, Nat. Phys. **7**, 239 (2011).

[25] W. Escoffier, C. Chapelier, N. Hadacek, and J.-C. Villégier, Phys. Rev. Lett. **93**, 217005 (2004).

[26] B. Sacépé, C. Chapelier, T. I. Baturina, V. M. Vinokur, M. R. Baklanov, and M. Sanquer, Phys. Rev. Lett. **101**, 157006 (2008).

[27] A. F. Andreev, Sov. Phys. JETP **19**, 1228 (1964).

[28] I. Giaever, Phys. Rev. Lett. **5**, 147 (1960).

[29] R. C. Dynes, V. Narayanamurti, and J. P. Garno, Phys. Rev. Lett. **41**, 1509 (1978).

[30] G. E. Blonder, M. Tinkham, and T. M. Klapwijk, Phys. Rev. B **25**, 4515 (1982).

[31] H. M. I. Jaim, J. A. Aguilar, B. Sarabi, Y. J. Rosen, A. N. Ramanayaka, E. H. Lock, C. J. K. Richardson, and K. D. Osborn, IEEE Trans. Appl. Supercond. **25**, 1 (2015).

[32] J. S. Chawla, X. Y. Zhang, and D. Gall, J. Appl. Phys. **113**, 063704 (2013).

[33] M. Gurvitch, Phys. Rev. B **24**, 7404 (1981).

[34] A. Roychowdhury, M. A. Gubrud, R. Dana, J. R. Anderson, C. J. Lobb, F. C. Wellstood, and M. Dreyer, Rev. Sci. Instrum. **85**, 043706 (2014).

[35] A. Roychowdhury, R. Dana, M. Dreyer, J. R. Anderson, C. J. Lobb, and F. C. Wellstood, J. Appl. Phys. **116**, 014308 (2014).

[36] M. Tinkham, *Introduction to Superconductivity* (Courier Dover Publications, 2012).

[37] See Supplemental Material at [URL will be inserted by publisher] for detailed explanation.

[38] N. Sharma, P. C. W. G. Vugts, C. Daniels, W. Keuning, J. T. Kohlhepp, O. Kurnosikov, and B. Koopmans, Nanotechnology **25**, 495201 (2014).

[39] S. H. Pan, E. W. Hudson, K. M. Lang, H. Eisaki, S. Uchida, and J. C. Davis, Nature **403**, 746 (2000).

[40] J. Bardeen, L. N. Cooper, and J. R. Schrieffer, Phys. Rev. **108**, 1175 (1957).

[41] R. Machunze and G. C. A. M. Janssen, Thin Solid Films **517**, 5888 (2009).

[42] P. C. J. J. Coumou, E. F. C. Driessen, J. Bueno, C. Chapelier, and T. M. Klapwijk, Phys. Rev. B **88**, 180505 (2013).

[43] A. Bruno, G. De Lange, S. Asaad, K. L. Van der Enden, N. K. Langford, and L. DiCarlo, Appl. Phys. Lett. **106**, 182601 (2015).

[44] D. P. Pappas, M. R. Vissers, D. S. Wisbey, J. S. Kline, and J. Gao, IEEE Trans. on Appl. Supercond. **21**, 871 (2011).

[45] L. Grünhaupt, N. Maleeva, S. T. Skacel, M. Calvo, F. Levy-Bertrand, A. V. Ustinov, H. Rotzinger, A. Monfardini, G. Catelani, and I. M. Pop, Phys. Rev. Lett. **121**, 117001 (2018).

[46] D. Cho, K. M. Bastiaans, D. Chatzopoulos, G. D. Gu, and M. P. Allan, Nature **571**, 541 (2019).